



A. Jaberi · M. Tadjfar

# Visualization of two-dimensional liquid sheets issued into subsonic gaseous crossflow

Received: 30 December 2019 / Revised: 25 February 2020 / Accepted: 19 March 2020 / Published online: 12 May 2020  
© The Visualization Society of Japan 2020

**Abstract** Flow dynamics of two-dimensional liquid sheets discharged into low-speed gaseous crossflow were experimentally investigated. The flow characteristics of liquid sheets were visualized by taking advantage of diffused backlight shadowgraphy and high-speed photography. Three injectors with an equal thickness of 0.35 mm and aspect ratios of 30, 60 and 90 were manufactured and tested at different flow conditions. A full discussion about the flow characteristics of two-dimensional liquid sheets in the presence of transverse airflow is provided. Visualizations revealed that the liquid sheets represented a unique concave-like structure that was named as inflated sheet. This special characteristic was not previously seen on any other circular or non-circular liquid jets and therefore made the flow dynamics of liquid sheets in subsonic crossflow very distinguished. The inflated sheet was found to transform from an enclosed structure into an open structure. The open inflated sheet was disturbed by different breakup mechanisms including sheet rupture, bag breakup, and Rayleigh–Taylor instability. Based on the observed phenomena, the flow was grouped into five regimes including biconvex, enclosed inflated sheet, open inflated sheet, bag breakup/sheet rupture, and multimode breakup. Furthermore, it was found that the droplet region was bifurcated due to the different breakup mechanisms acting simultaneously upon the sheet. Measurements of sheet trajectory were performed and the effects of momentum ratio and Weber number were studied. It was found that Weber number was only effective at low values, while momentum ratio remarkably impacted the trajectory.

**Keywords** Two-dimensional injectors · Liquid sheets · Transverse airflow · Inflated sheet · Biconvex structure

## 1 Introduction

The perpendicular injection of a liquid jet into gaseous airflow is a fundamental problem that its applications range from thermal spray coating to the combustion of aeroengines (Jadidi et al. 2019; Wu et al. 2016). The flow dynamics of liquid jets in crossflow (JICF) is very complicated as it is associated with several instabilities such as Kelvin–Helmholtz, Rayleigh–Taylor and Plateau-Rayleigh that simultaneously act on the fluid flow (Broumand and Birouk 2017). Numerous studies have been conducted to explore the different flow characteristics of JICF including flow regimes, breakup features, jet trajectory, penetration height, droplet size distribution, to name a few (Amighi and Ashgriz 2019; Broumand and Birouk 2019; Chen et al. 1993; Sallam et al. 2004; Wu et al. 1997). The general structure of a liquid jet in crossflow has been mostly categorized into three regions: liquid core, ligament region and droplet or atomized region. The liquid core region is the unbroken part of the liquid that is emanated from the injector. Several disturbances grow along

---

A. Jaberi · M. Tadjfar (✉)  
Turbulence and Multiphase Flow Laboratory, Department of Aerospace Engineering, Amirkabir University of Technology, Tehran, Iran  
E-mail: mtadjfar@aut.ac.ir

the liquid column until finally breaks up. Depending on the flow conditions, liquid segments (ligaments) and droplets disintegrate from the liquid column and form the ligament region. These ligaments go through a secondary breakup, due to the shear force from the airflow, and rupture into smaller droplets.

Many different factors are important in determining the flow characteristics of JICF. However, the geometry of liquid jets was found to be one of the most effective ones that can significantly alter the dynamics of the liquid jet. Indeed, in the recent decade, great attention was given to the injectors with non-circular exit shapes. This was mostly due to the fact that non-circular shapes bring in new physics to the flow and thus can be implemented as passive flow controllers. Breakup and axis-switching characteristics of elliptical liquid jets discharged into quiescent air were investigated by several studies (Amini and Dolatabadi 2011; Jaber and Tadjfar 2020; Kasyap et al. 2009; Muthukumaran and Vaidyanathan 2014; Pillai et al. 2014). It was revealed that due to the occurrence of axis-switching elliptical jets were less stable than the circular jets and disintegrated earlier. Moreover, the wavelength and amplitude of the axis-switching phenomenon were fully examined and their variations with flow conditions were experimentally and theoretically studied. Wang and Fang (2015) studied the influence of geometry by implanting four orifices with circular, rectangular, triangular and square cross-sections. Their visualizations revealed that axis-switching also happened for rectangular jets. A comprehensive study on rectangular jets was performed by Tadjfar and Jaber (2019). Taking advantage of six injectors with different aspect ratios varying from 1 to 6, the development of rectangular liquid jets was fully considered. Following this work, Jaber and Tadjfar (2019b) presented a theoretical analysis to predict the wavelength and frequency of elliptical and rectangular liquid jets.

Similar to the studies performed on non-circular liquid jets in stagnant air, growing attention was recently emerged to examine these jets in transverse airflow. The goal is to control and optimize the mixing of liquid and gas flows in a way to achieve desirable characteristics. Prakash et al. (2014) studied the breakup of pressure swirl jet in the presence of gaseous crossflow. Visualizing the flow dynamics of pressure swirl jet at different flow conditions, they could identify five different regimes. Zhang et al. (2018) experimentally investigated the flow of a hollow cone spray injected into the gaseous crossflow. In this work, the regular parameters of JICF were not measured and instead the focus was given to the vortex structure formed by the droplets. Shadowgraph imaging was used by Jadidi et al. (2019) to visualize the elliptical liquid jets in transverse airflow. They used several elliptical injectors with different aspect ratios and studied the trajectory, bag formation, and breakup features. Trajectory of elliptical liquid jets was investigated in more detail by Song et al. (2019). Using backlight photography, they could measure the upper boundary and centerline of the liquid jet before the point of breakup. Based on their results, they proposed several empirical equations to describe the jet trajectory. Aside from elliptical jets, rectangular liquid jets were also examined in the presence of gaseous crossflow. Tadjfar et al. (2019) used four rectangular injectors with aspect ratios of 1, 2, 3 and 4. Based on the observations, they categorized the liquid flow into four regimes and also measured the jets' trajectory at different momentum ratios and Weber numbers.

It was seen that a tendency toward using non-circular jets has emerged in recent years. For liquid jets in crossflow, employing non-circular liquid jets might lead to the improvement of spray characteristics. In this study, two-dimensional liquid sheets were discharged into subsonic crossflow for the first time. Due to the sheet nature of the liquid flow, its interaction with the transverse airflow would become much more intense, and it would be shown that the flow characteristics are highly different than circular or other non-circular liquid jets. The flow field of two-dimensional liquid sheets in stagnant air was previously studied by the authors and unique phenomena were identified (Jaber and Tadjfar 2019a). Some of these new phenomena were briefly discussed in this study as they have a profound effect on the flow dynamics of two-dimensional liquid sheets in crossflow.

## 2 Experimental method

A schematic diagram of the test facility is presented in Fig. 1. As seen, the experimental setup was comprised of three parts, including, the pressurized liquid injection system, wind tunnel, and high-speed photography system. According to Fig. 1a, a high-pressure nitrogen capsule was used to apply uniform gas pressure upon the water stored in a tank with a capacity of 70 L. Undesirable interactions between high-pressure nitrogen and liquid water were avoided by taking advantage of a baffle that was placed at the nitrogen gas inlet. During all tests, the gauge pressure applied over the liquid tank was fixed at 5 bar.

Further, the storage tank was equipped with a safety pressure relief valve. Water flow rate was controlled and measured via a Rotameter-type flowmeter that its accuracy was found to be around  $\pm 0.15$  LPH. Experiments were performed in the multiphase flow wind tunnel of the Aerospace Department of Amirkabir University. A 3D isometric view of the wind tunnel is provided in Fig. 1b. It is in an open-circuit wind tunnel with a maximum air velocity of 45 m/s. The air speed of the wind tunnel was adjusted using an inverter that was monitored and controlled online via a computer. This wind tunnel owns a test section with a rectangular cross-section of  $300 \times 300$  mm<sup>2</sup> and a length of 1300 mm. Glass plates were attached to both sides of the wind tunnel test section to provide optical access. The roof of the test section was made from Teflon and a hole was cut through it for the accommodation of the injector assembly. The mixture of sprayed

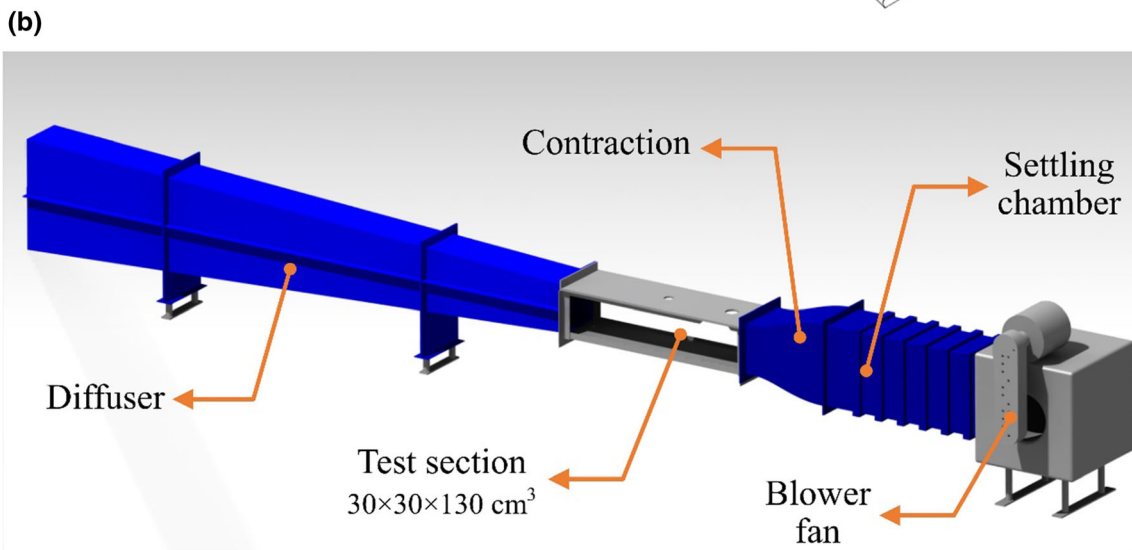
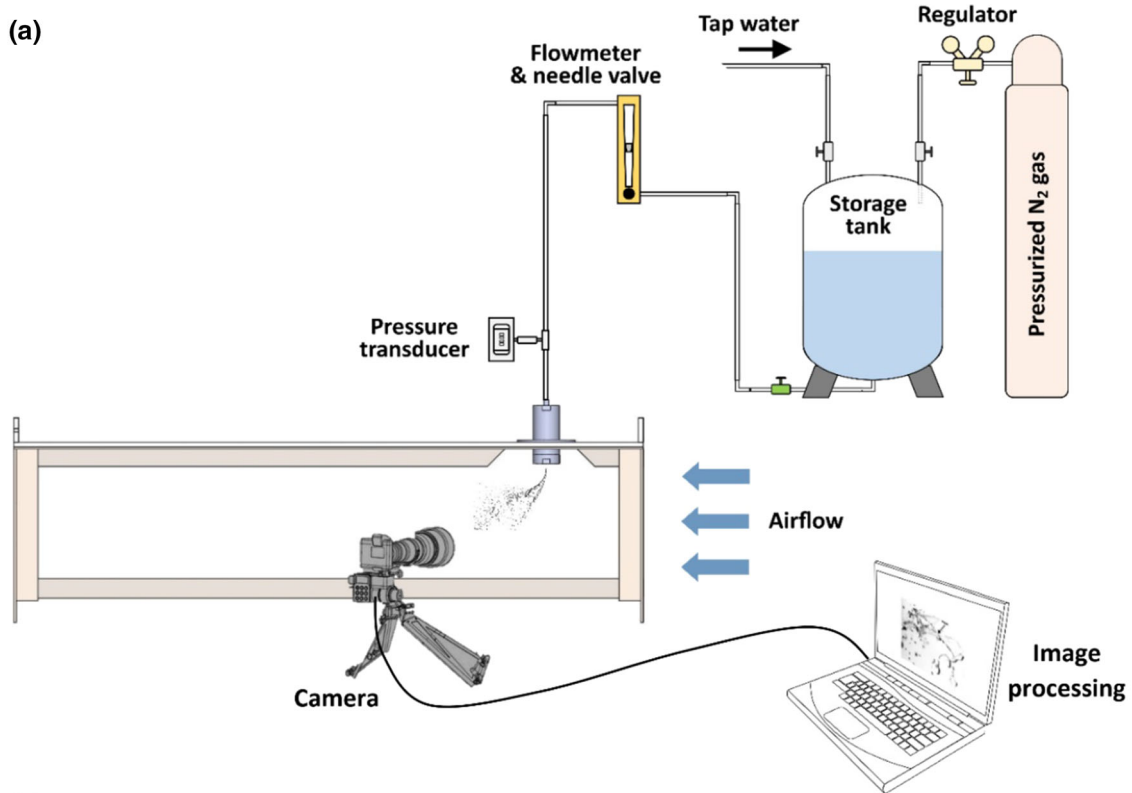


Fig. 1 Schematic of the experimental setup. a Liquid injection and imaging systems, b wind tunnel

water and air stream was finally released into the free environment through a long diffuser, outside of the laboratory.

To produce two-dimensional liquid sheets, slits with high aspect ratio and very thin thickness were constructed. The material used for manufacturing the injectors was stainless steel, and they were drilled by electro-discharge machining (EDM) method, which can assure the highest precision of the machining. Three injectors with different widths and an equivalent thickness of 0.35 mm were manufactured. A summary of the injector's geometry is given in Table 1. These injectors were indexed as TD1, TD2 and TD3. According to Table 1, the aspect ratios of these injectors were 30, 60 and 90, respectively. The liquid flow was first forced into a cylindrical settling chamber with a length of 80 mm and a diameter of 45 mm before it was fed to the injector. The configuration of the settling chamber and injector assembly is presented in Fig. 2.

In order to visualize the physics of the two-dimensional liquid sheets issued into gaseous crossflow, diffused backlight shadowgraphy was employed. In this technique, the light source illuminates the background of the liquid sheet and a camera takes photographs from the opposite direction. For this study, two high lumen LEDs were used to illuminate the background of the liquid sheet. The shedding light was uniformly distributed by means of an optical diffuser. To take photographs from the liquid sheets, a Nikon 1 J4 digital camera equipped with a Macro-NIKKOR AF-S 60 mm f/2.8 G lens was used. This camera can record photographs with 60 fps, 120 fps, 400 fps and 1200 fps at pixel resolutions of  $5322 \times 3488$ ,  $1280 \times 720$ ,  $768 \times 288$  and  $416 \times 144$ , respectively. Within all the experiments, the exposure time was set to  $1/16000$ s, which was small enough to freeze the dynamic of the liquid sheets.

Tap water was used as the working liquid and its properties at room temperature ( $25^\circ \sim 30^\circ$ ) were:  $\rho_l = 995 \text{ kg/m}^3$ ,  $\mu = 0.802 \times 10^{-3} \text{ kg/ms}$  and  $\sigma = 0.0728 \text{ N/m}$ . Moreover, the density of air at room pressure and temperature was  $\rho_g = 1.225 \text{ kg/m}^3$ . The flow dynamics of a liquid sheet discharged into gaseous crossflow is significantly governed by the liquid/gas momentum ratio ( $q$ ), that is defined as:

$$q = \frac{\rho_l v_j^2}{\rho_g u_g^2} \quad (1)$$

in which,  $v_j$  and  $u_g$  represent the liquid sheet exit velocity and transverse air speed, respectively. In the present study, the momentum ratio was varied from 30 to 150. This range was chosen to cover all the flow regimes of the liquid sheet in crossflow. In order to obtain a comprehensive understanding of the liquid flow, at each momentum ratio, the liquid volume flow rate was changed from  $20 \text{ L/h}$  to  $120 \text{ L/h}$ ; this resulted in a wide range of liquid exit velocities ranging from  $0.50 \text{ m/s}$  to  $9 \text{ m/s}$  and air velocities of  $2 \text{ m/s}$  to  $35 \text{ m/s}$ . The flow conditions of liquid sheets in gaseous crossflow are usually described by liquid jet Weber number ( $We_j$ ) and gas Weber number ( $We_g$ ) as following:

$$We_j = \frac{\rho_l v_j^2 t_H}{\sigma} \quad (2)$$

$$We_g = \frac{\rho_g u_g^2 t_H}{\sigma} \quad (3)$$

wherein  $t_H$  is the thickness of the two-dimensional sheets and  $\sigma$  is the surface tension of the liquid. Based on the flow conditions, the  $We_j$  and  $We_g$  were varied from 1.2 to around 400 and 0.01 to 13.1, respectively. In Fig. 3, the variations of gas and jet Weber numbers with liquid exit velocity are given. It must be noticed that by changing of momentum ratio, the jet Weber number remains constant, while the gas Weber number increases with the decrease in momentum ratio.

**Table 1** Geometric parameters of the injectors

Injector	Thickness (mm)	Width (mm)	Nozzle exit area (mm <sup>2</sup> )	Aspect ratio
TD1	0.35	10.5	3.675	30
TD2	0.35	21.0	7.350	60
TD3	0.35	31.5	11.025	90

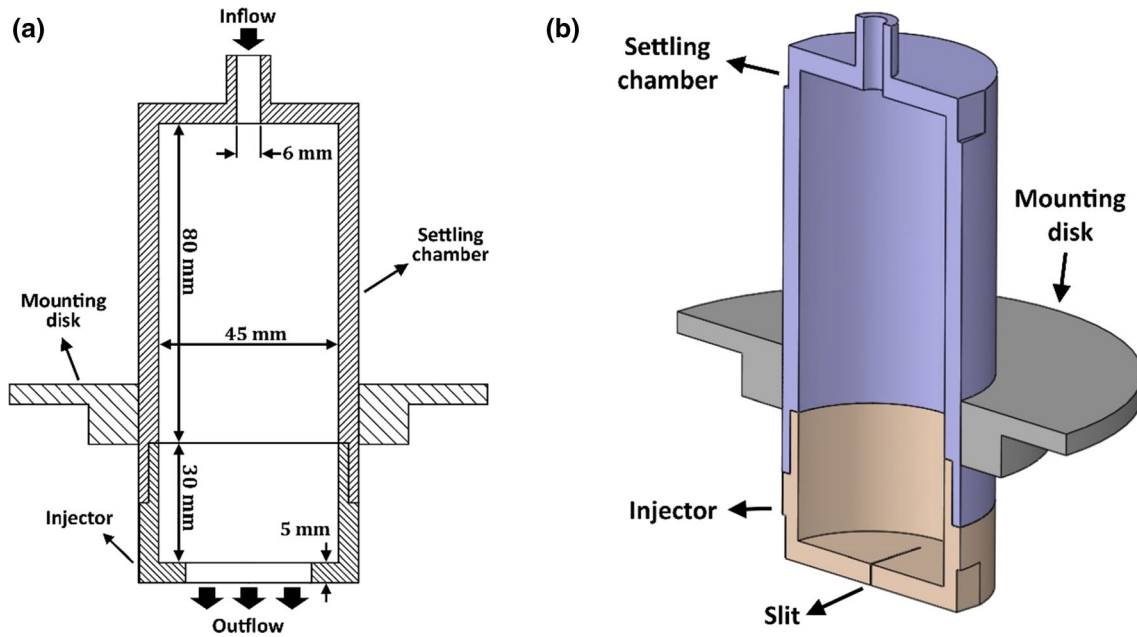


Fig. 2 Geometry details of the settling chamber and injector assembly, **b** 3D isometric view

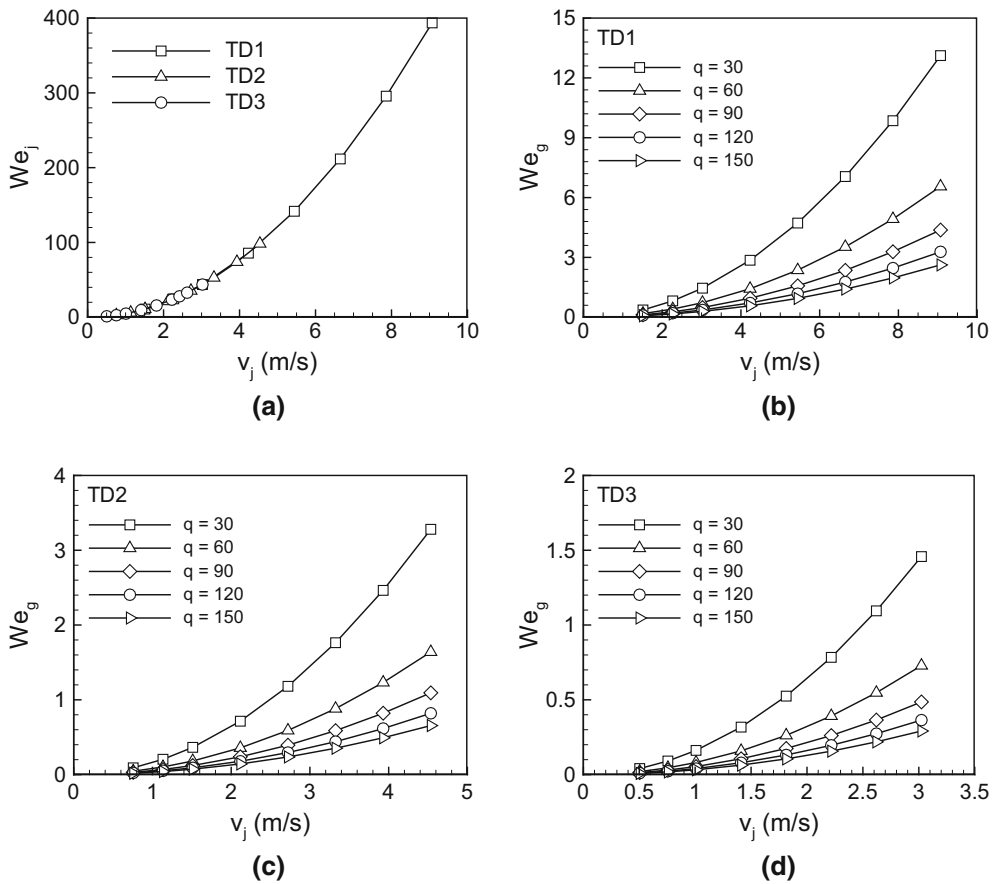


Fig. 3 Variation of gas and jet Weber numbers. **a** Jet Weber number, **b** gas Weber number of TD1, **c** gas Weber number of TD2 and **d** gas Weber number of TD3

### 3 Results and discussion

The injection of a liquid jet into transverse gaseous crossflow results in a highly complicated interaction between two fluids. The liquid jet blocks the air flow and consequently, a pressure difference between the windward and leeward sides of the liquid jet is created. This pressure difference leads to the flattening, deformation and bending of the liquid jet. Depending on the flow condition, different flow regimes and breakup mechanisms would appear over the sheet. In this study, the flow dynamics of two-dimensional liquid sheets injected into gaseous crossflow was qualitatively explored through the visualizations taken at different flow conditions. Further, a brief summary of the flow characteristics of two-dimensional liquid sheets in quiescent air is also given.

#### 3.1 Liquid sheets in quiescent air

Before testing in gaseous crossflow, it was necessary to examine the flow dynamics of the two-dimensional liquid sheets injected into stagnant air. This was important as the flow characteristics of the liquid sheets when issued into the gaseous crossflow could be better understood. Therefore, in this section, a brief discussion would be given about the flow features of two-dimensional liquid sheets in stagnant air. In Fig. 4, the flow development of TD1 sheet with increase in jet Weber number is given. At low Weber numbers, the inertia force is not significant, and the fluid flow was governed by surface tension and gravity forces. As shown in Fig. 4a, the flow is in dripping regime at which the liquid was disintegrated right from the exit plane as spherical drops. At higher jet Weber numbers, the flow entered the columnar regime. In this regime, surface tension force was so dominant that could accumulate all the liquid leaving the injector and form a liquid column (Fig. 4b). This column flowed downstream similar to a regular circular liquid column until finally disintegrated due to the Plateau-Rayleigh instability. However, in spite of the rather low velocity, the surface of the liquid column was not as smooth as would have been for circular or non-circular liquid jets at the same velocities (Jaber and Tadjfar 2019b; Tadjfar and Jaber 2019). Apparently, the work of surface tension to accumulate the liquid induced additional disturbances into the flow and made its surface perturbed.

Changing the liquid velocity to higher values, the inertia became gradually comparable with other forces and remarkably altered the fluid flow. As shown in Fig. 4c, a triangular sheet was formed downstream of the exit plane. In the triangular regime, the liquid was discharged all along the sheet width and established a sheet. However, the surface tension acted on the edges and pulled them back inward. Retraction of sheet boundaries led to the formation of thick rims over the triangular sheet. These rims became thicker with further traveling of the liquid downstream and converged toward the central axis of the sheet. It was noticed that the liquid between the rims remained thin and two-dimensional, even though disturbed by crisscrossing waves that were emanated from the rims. Triangular regime was found to be the main regime of the two-

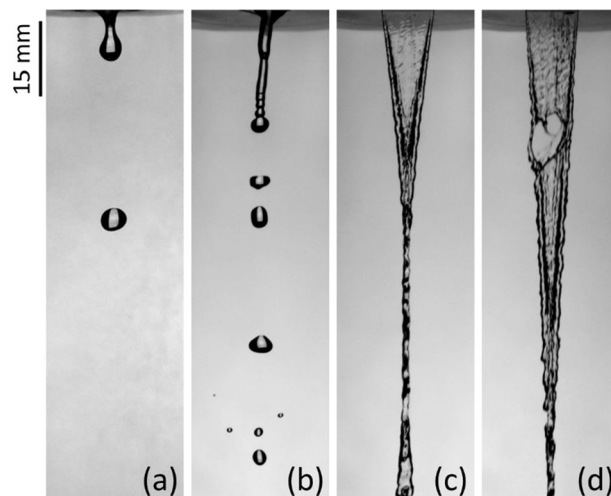


**Fig. 4** Flow regimes of two-dimensional liquid sheets when injected into still air. Photographs taken from TD1. **a** Dripping regime,  $We_j = 0.25$ , **b** columnar regime,  $We_j = 0.98$ , **c** triangular regime,  $We_j = 112$ , and **d** perforation regime,  $We_j = 394$



dimensional. Indeed, the injection velocities tested in the presence of transverse airflow were limited to the ones corresponding to the triangular regime. However, at high enough velocities, the liquid sheet surface was perturbed by instabilities that emerged due to the turbulence of the liquid flow. These instabilities somehow led to the occurrence of local perforation across the triangular sheet (Fig. 4d). The perforation then grew in size due to work of surface tension until eventually became big enough to reach the rims and then breaking up. The flow conditions corresponding to the perforation regime were not tested in the presence of gaseous crossflow.

The flow features of the two-dimensional liquid sheets were also examined from the orthogonal view. As shown in Fig. 5, both front and side views of TD2 sheet at the injection velocity of 2.12 m/s, corresponding to the  $We_j = 21.4$  are given. It is clearly observed in this figure that the liquid flow is in the triangular regime. The side view snapshot shows that at the bottom of the triangular sheet, the converging rims collided to each other and formed a biconvex structure at the orthogonal plane. The biconvex structure created by the collision of thickened rims was similar to the flow structure generated in the impingement of two circular liquid jets (Li and Ashgriz 2006). The biconvex structure was itself surrounded by thick wavy rims. These waves were induced through the rims due to disturbances that were generated by the collision of the primary sheet rims. The surface tension eventually closed the biconvex structure and at more downstream, a ruffled column of liquid was established.

A brief description of the two-dimensional liquid sheets discharged into quiescent air was provided as it was necessary to interpret the physics of the fluid flow when injected into gaseous crossflow. These features play an important role in the flow dynamics of the two-dimensional liquid sheets in the presence of perpendicular airflow, which would be discussed in the following sections.

### 3.2 Flow dynamics of liquid sheets in crossflow

In the previous section, the main features of two-dimensional liquid sheets in quiescent air were briefly described. In this section, visualizations are given for the liquid sheets in the presence of transverse airflow. Initially, the effect of flow conditions on the physics of two-dimensional sheets was investigated and then the flow dynamics of all three injectors were compared to each other.

Even though the effect of momentum ratio on the flow dynamics of liquid sheets injected into subsonic crossflow has been emphasized by previous studies (Birouk et al. 2003; Eslamian et al. 2014; Wu et al. 1997), but changing Weber number has also a significant influence on the sheet characteristics. For keeping the momentum ratio constant, both jet Weber number and gas Weber number change in accordance with

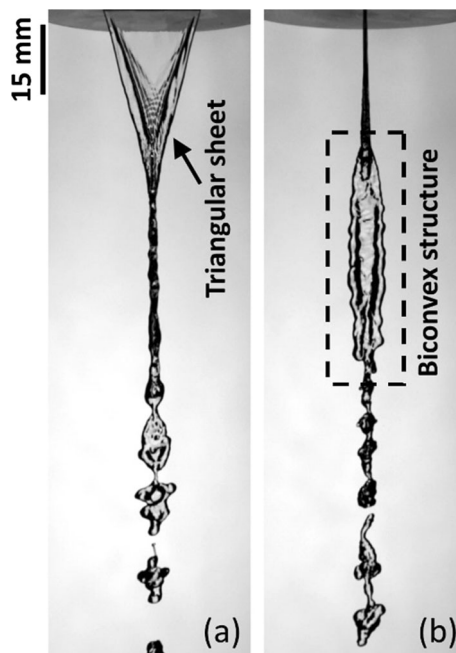
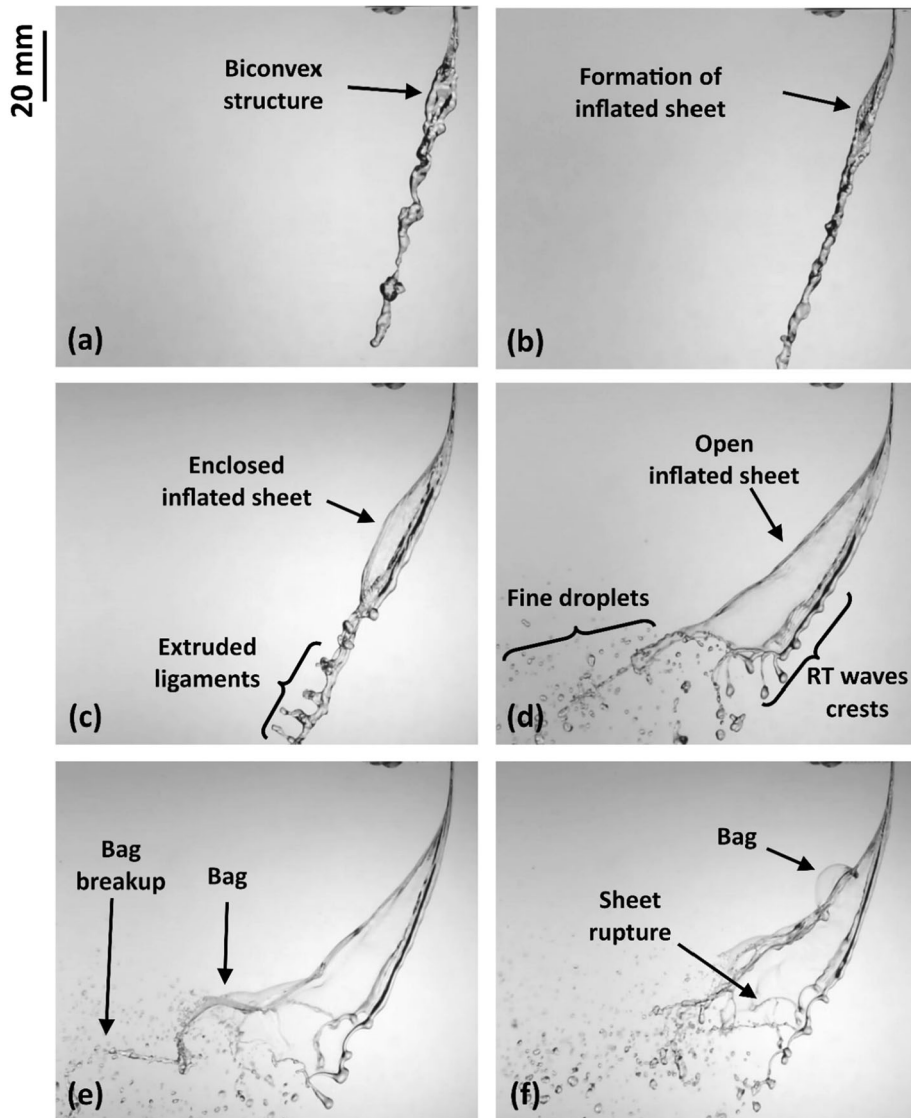


Fig. 5 TD2 liquid sheet at  $We_j = 21.4$ . **a** Front view, **b** side view

each other. To study the effect of Weber number, the flow visualizations of TD3 sheet are given at different Weber numbers while keeping the momentum ratio fixed.

Among the three fabricated injectors, TD3 was the one with the highest aspect ratio, 90, and therefore it can be considered as the most two-dimensional sheet compared to TD1 and TD2 with aspect ratios of 30 and 60, respectively. The visualization of this sheet at the constant momentum ratio of 120 and different gas and jet Weber numbers are given in Fig. 6. All the photographs presented in Fig. 6 are of the same scale, so a comparison between the TD3 sheet at different flow conditions became feasible. Following the sequence of photographs clearly shows the alteration of liquid sheet structure with the changing of Weber number. In Fig. 6a, the  $We_g$  was very low, and therefore the liquid sheet was not perceptibly influenced by the presence of airflow. The liquid sheet was slightly bent in the air direction, while the biconvex structure was vividly observed downstream of the injection plane. Indeed, the aerodynamic drag force exerted upon the sheet was not strong enough to affect its structure and the biconvex structure remained nearly intact. However, the instabilities leading to the breakup of the liquid sheet might have been intensified by the transverse airflow.

Gradually increasing both  $We_j$  and  $We_g$ , the biconvex structure was flattened and then diminished. In fact, in Fig. 6b, there is no sign of the biconvex structure anymore. Instead, a unique phenomenon appeared



**Fig. 6** Flow dynamics of TD3 sheet at the momentum ratio of 120 and for different Weber numbers. **a**  $We_j = 2.73$ ,  $We_g = 0.02$ , **b**  $We_j = 9.52$ ,  $We_g = 0.08$ , **c**  $We_j = 15.7$ ,  $We_g = 0.13$ , **d**  $We_j = 23.5$ ,  $We_g = 0.20$ , **e**  $We_j = 32.8$ ,  $We_g = 0.27$ , and **f**  $We_j = 43.7$ ,  $We_g = 0.36$



over the two-dimensional liquid sheet. The aerodynamic force exerted upon the windward side of the liquid sheet was high enough so that the sheet was stretched and expanded in the air flow direction, forming a phenomenon that was named by the authors as the “inflated sheet.” This new phenomenon can better be seen in Fig. 6c with higher air velocity. It must be noticed that the inflated sheet is different from bags that are usually seen over liquid sheets in crossflow. Bags are local bumps that appear over the liquid jet and expand along with it until finally bursting at downstream. In contrast, the inflated sheet is a steady structure that begins in the vicinity of the exit plane and continues in the flow until the point of rupture. The onset of the inflated sheet was first manifested as a small expansion for the flow condition of Fig. 6b. The size of the inflated sheet is grown in Fig. 6c, where a big bump was established over the liquid sheet, enclosed by thick rims. These rims and the inflated sheet were all merged together and formed a liquid column. As highlighted in Fig. 6c, the liquid column following the inflated sheet became highly ruffled and long ligament-like overshoots perpendicular to its trajectory were extruded. The formation of these extrusions can be attributed to the lateral inertia that was generated by the collision of rims around the inflated sheet. This lateral inertia resulted in overshoots that were then more stretched by the wind force.

With the increase in Weber number, the shape of the inflated sheet was significantly altered. Presented in Fig. 6d, the size of the inflated sheet remarkably expanded because of the greater pressure difference between the windward and leeward sides of the sheet. Moreover, the inflated sheet was no longer surrounded by rims and instead was ruptured at downstream. The rupturing of the inflated sheet happened as a result of its expansion. When fully expanded, the sheet membrane became very thin and surface tension no longer could hold it attached. A magnified view of sheet rupture is shown in Fig. 7 for TD3 sheet at the momentum ratio of 100 and  $We_j = 52.9$ . In this figure, it was shown that the inflated sheet was ruptured from rim to rim. Moreover, at the edge of sheet rupture, the liquid was pulled back by the surface tension force and formed another rim. This thinner rim is highlighted in Fig. 7. Inflated sheet rupture was used as a criterion to categorize the inflated sheet into enclosed (without rupture, Fig. 6c) and open (with rupture, Fig. 6d). Fine droplets were generated through the rupturing of the inflated sheet which formed the upper boundary of the droplet region. The release of these droplets was greatly visualized in Fig. 7. The lower boundary was made of bigger droplets that were separated from the nodes along the sheet rims. These nodes were developed due to the Rayleigh–Taylor instability mechanism (Sallam et al. 2004; Tan et al. 2018). When both pressure and density gradients exist at the interface of two fluids, two counter-rotating vortices will be created that perturb the interface shape into a wave-like pattern. These surface waves were clearly seen over the sheet rims in Fig. 6d. The amplitude of these waves was increased along the rim. Once the liquid mass carried through these nodes became high enough, the surface tension accumulated the liquid into a sphere-like shape. Afterward, the Plateau-Rayleigh instability broke up these nodes from the sheet and released bigger droplets into the air flow. Accordingly, it can be observed that the droplet region was bifurcated into two branches. The upper branch with smaller droplets emerged due to sheet rupture and the lower branch with bigger droplets formed because of the nodes breakup. These two branches were separated from each other by an in-between region, in which the presence of droplets was less dense. Further increase in Weber number was followed by the appearance of bags over the inflated sheet. These bags are spotted in Fig. 6e and f, as local bumps over the inflated sheet. Further, the disintegration of these bags can also be observed downstream. It was found that with more increase in Weber number, the formation of bags became more frequently and also closer to the injection plane. At these flow conditions, both sheet rupture and bag breakup existed simultaneously.

The flow visualizations of the TD3 sheet at the lower momentum ratio of 30 are provided in Fig. 8. Due to the lower momentum ratio, the gas effects on the liquid sheet were intensified in comparison to Fig. 6. Again, all the photographs are of the same scale to make a qualitative comparison possible. The flow development observed for the momentum ratio of 120 was more or less identified at this momentum ratio. However, some differences were noticeable that would be discussed in the following. At the lowest  $We_j$  shown in Fig. 8a, the biconvex structure was much smaller and hardly could be recognized. Indeed, as the aerodynamic forces were stronger, the biconvex structured started to diminish at lower jet Weber numbers. With slightly changing the Weber number to higher values, the inflated sheet structure was soon established. As shown in Fig. 8b, the enclosed inflated sheet can clearly be recognized. Moreover, the liquid column following the inflated sheet was disintegrated through Rayleigh-Plateau mechanism, since spherical droplets were formed and shed into the crossflow. At this momentum ratio, the transition from enclosed inflated sheet to open inflated sheet happened at a lower jet Weber number. In Fig. 8c, with the  $We_j = 15.7$ , the fluid flow entered the open inflated sheet regime. Comparing to the visualizations of Fig. 6, indicated that gas Weber number was more influential in determining the flow physics of the two-dimensional liquid sheets. More

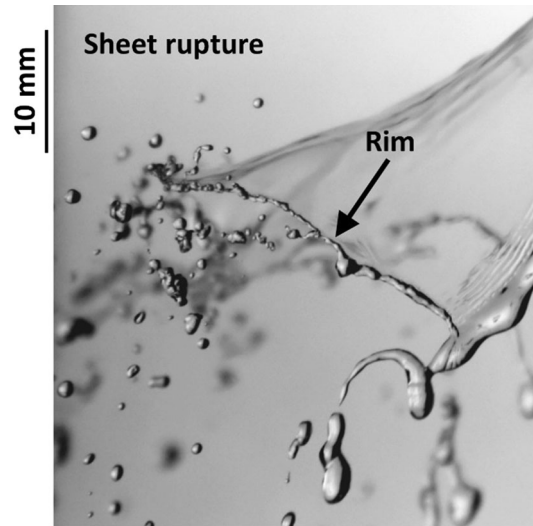


**Fig. 7** A magnified view of sheet rupture for TD3 sheet at  $q = 100$ ,  $We_j = 52.9$  and  $We_g = 0.53$

interesting, it was found that bags also appeared upon the inflated sheet at this flow condition. Bag formation and breakup are well-captured and highlighted in Fig. 8c.

Increasing the gas Weber number to 0.78, the disintegration of the liquid sheets became more intense. As shown in Fig. 8d, the liquid sheet was highly influenced by the bag breakup and sheet rupture. Also noticeable from the photo, bag breakup was more prominent. More importantly, the bifurcation behavior shown in Fig. 6, with the momentum ratio of 120, was also identified here. The upper branch was formed from the fine droplets released due to bag breakup and sheet rupture. On the lower part, a combination of ligaments and big droplets was present; droplets that were produced through the Rayleigh–Taylor instability acting on the sheet rims. With more increase in gas Weber number (Fig. 8e), the aerodynamic effects got more strong on the liquid sheets and the atomization process became accelerated. As a consequence, the space between the upper and lower branches was smaller. At the highest tested Weber number, the frequency of bag formation and breakup increased so that a clear distinction between different bags was not possible anymore. A sequence of bags are shown by an arrow in Fig. 8f where several bags were formed immediately downstream of the exit plane. Furthermore, the droplet region reached a uniformity, and the bifurcation was no longer recognizable. This was due to the high frequency of breakups that generated a nearly uniform region of droplets. It must be noticed that at higher air velocities, the shear force between liquid and air flows becomes stronger and then owing to the Kelvin–Helmholtz instabilities, surface breakup gradually occurs.

### 3.3 Detailed inspection of inflated sheet formation

Since the inflated sheet structure was the main feature of the two-dimensional liquid sheets in crossflow, a closer look at its formation seemed to be necessary. Testing at high-momentum ratios from 500 to 80, corresponding to gas Weber numbers from 0.02 to 0.15 and at the constant jet Weber number of 15.7, an accurate evaluation of the inflated sheet development was provided. Following the visualizations of Fig. 9, it appeared that the development of the inflated sheet was simultaneous with the diminishing of the biconvex structure. Given in Fig. 9a, the biconvex structure was identified immediately below the collision point of the triangular sheet rims. Yet, there was no perceptible sign of the inflated sheet formation. However, the biconvex structure, itself, was slightly influenced by the gaseous crossflow. In Fig. 5b, it was shown that both sides of the biconvex structure were surrounded by thick rims. This is while, in the presence of airflow, Fig. 9a, it seemed that the rear rim was still thick enough to be clearly observed, whereas the front one appeared to be diminished. This was attributed to the pressure distribution around the biconvex structure. In fact, after reaching the stagnant condition at the rear point of the liquid sheet, the airflow accelerated along the sides of the biconvex structure and thus the pressure was dropped. This reduction in side pressure allowed the liquid to get thicker in the sidewise direction. As a result of liquid thickening, the front rim was merged into the liquid. This can be better demonstrated by following Fig. 9a, b, as with the increase in  $We_g$

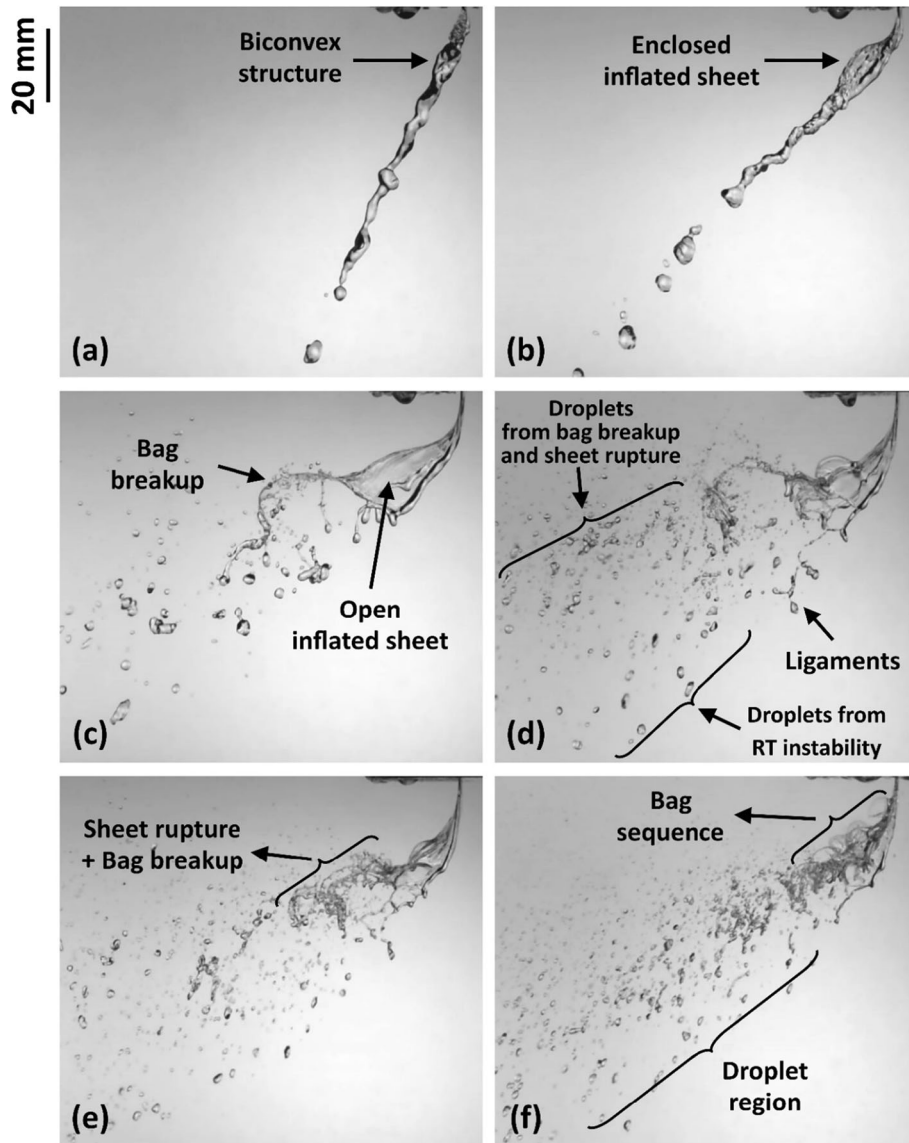


**Fig. 8** Flow dynamics of TD3 sheet at the momentum ratio of 30 and for different Weber numbers. **a**  $We_j = 2.73$ ,  $We_g = 0.09$ , **b**  $We_j = 4.86$ ,  $We_g = 0.16$ , **c**  $We_j = 15.7$ ,  $We_g = 0.52$ , **d**  $We_j = 23.5$ ,  $We_g = 0.78$ , **e**  $We_j = 32.8$ ,  $We_g = 1.09$ , and **f**  $We_j = 43.7$ ,  $We_g = 1.46$

the width of the biconvex structure was shrunk. It must be noticed that the conservation of mass necessitates the thickening of the biconvex structure.

The first perceptible sign of the inflated sheet birth is observed in Fig. 9b. According to the figure, the inflated sheet started to establish in the proximity of the lower part of the triangular sheet, where rims were converged toward the central axis and collided with each other. Development of the inflated sheet was due to the pressure difference between the windward and leeward sides of the triangular liquid sheet. On the other hand, the longitudinal inertia of the liquid flow opposed the pressure force and prohibited it from affecting the liquid sheet. That is why in the vicinity of the exit plane, the liquid sheet was not even bent in airflow direction. However, at downstream, about the rims collision point, the cross sectional area of the liquid was increased due to the formation and convergence of rims and thus its velocity was decreased. As a result, the force exerted upon the liquid flow from the pressure difference became comparable with inertia and could affect the flow. The point of inflated sheet establishment was therefore governed by the balance between the inertia and aerodynamic drag force. As given in Fig. 9c, with more increase in gas Weber number, the inflated sheet was expanded more. Moreover, the biconvex structure was nearly diminished so that a small

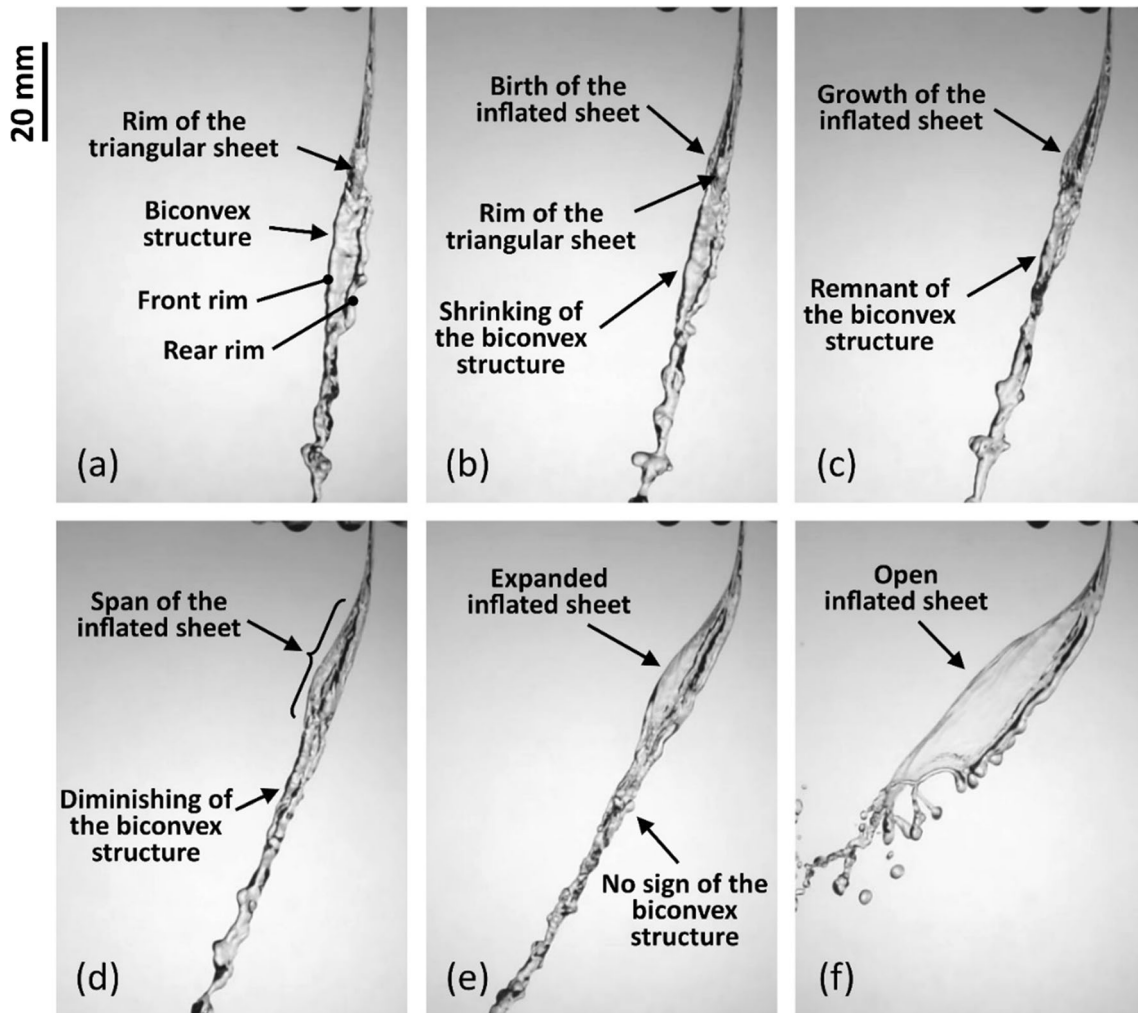


**Fig. 9** Illustration of the biconvex structure metamorphosis into inflated sheet. Photographs taken from TD3 sheet at  $We_j = 15.7$  and **a**  $q = 500$ ,  $We_g = 0.02$ , **b**  $q = 300$ ,  $We_g = 0.04$ , **c**  $q = 200$ ,  $We_g = 0.06$ , **d**  $q = 160$ ,  $We_g = 0.07$ , **e**  $q = 120$ ,  $We_g = 0.1$ , and **f**  $q = 80$ ,  $We_g = 0.15$

remnant of it was left. This trend is continued in Fig. 9d, e with gas Weber numbers of 0.07 and 0.1, respectively. As seen, the inflated sheet was highly expanded and more spanned upstream and downstream of the liquid flow. However, the growth of the inflated sheet seemed to be more in the downstream direction. Furthermore, the biconvex structure was completely diminished and absorbed into the inflated sheet so that no sign of it could be identified in Fig. 9e with the momentum ratio of 120. At last, by lowering the momentum ratio to 80, as in Fig. 9f, the inflated sheet was fully expanded and ruptured at downstream. As was previously stated, when the inflated sheet was ruptured, the flow regime has entered the open inflated sheet.

To better understand the geometry of the inflated sheet structure, a series of photographs were taken from a 60 deg. view angle. These visualizations were found very useful to give a detailed description of the inflated sheet development. Given in Fig. 10, shadowgraphs of TD3 sheet at the momentum ratio of 100 and for different Weber numbers are provided. Both the triangular sheet and biconvex stricter are shown in Fig. 10a, wherein the gas velocity was not high enough to highly alter the fluid flow. The inflated sheet is shown in Fig. 10b by which it was revealed that the triangular sheet played a critical role in the formation of the inflated sheet. According to this figure, the region between the rims of the triangular sheet was stretched into the airflow by the aid of the aerodynamic force. At the same time, the rims were not bent that much and remained behind the sheet, forming the concave shape of the liquid flow. In fact, rims carried more liquid and were heavier than the sheet between them, thus they were less bent by the force from the airflow. Also



notable from Fig. 10b, rims were merged with each other at downstream, closing the inflated sheet structure. Increasing the gas Weber number to 0.1 (Fig. 10c), the rims were detached from each other, allowing the inflated sheet to expand more in the airflow. Furthermore, it was seen that the span of the inflated sheet is remarkably elongated in Fig. 10c. Following the photographs of Fig. 10d–f, the distance between the rims was increased to a maximum and then remained nearly unchanged. The length of the inflated sheet was not elongated anymore since the sheet rupture occurred at downstream of the inflated sheet as displayed in Fig. 9d, e. Moreover, at higher Weber numbers (Fig. 10f) bags were appeared over the top surface of the inflated sheet.

### 3.4 Effect of liquid sheet aspect ratio

In Fig. 11, the visualizations of TD1 sheet at the constant momentum ratio of 150 are given. As given in Table 1, the aspect ratio of this injector was 30, which was minimum of the three injectors. Due to the lower area of TD1 compared to TD3, the  $We_j$  was higher at the same volumetric flow rate and consequently, at a constant momentum ratio, the gas Weber number was also higher. Also, provided in the caption of Fig. 11, the  $We_j$  and  $We_g$  varied between 10.9 to 212 and 0.07 to 1.41, respectively. All the photographs given in Fig. 11 are of the same scale, so a comparison between the photographs would be possible. Similar to the visualizations of TD3 sheet, the sequence of photographs clearly showed that the physics of the liquid sheet was highly altered by changing of Weber number. Further, the main features are those observed and discussed for the TD3 sheet, thus the description would be brief. In Fig. 11a, the sheet was negligibly influenced by the airflow and only was slightly bent. At this condition, the biconvex structure was still observable. At higher Weber numbers (Fig. 11b), the biconvex structure was in the middle of shrinking and the inflated sheet was just recognized. Presented in Fig. 11c, the inflated sheet was formed and fully expanded. Sheet rupture was shown in the photograph and the Rayleigh–Taylor instabilities were observed

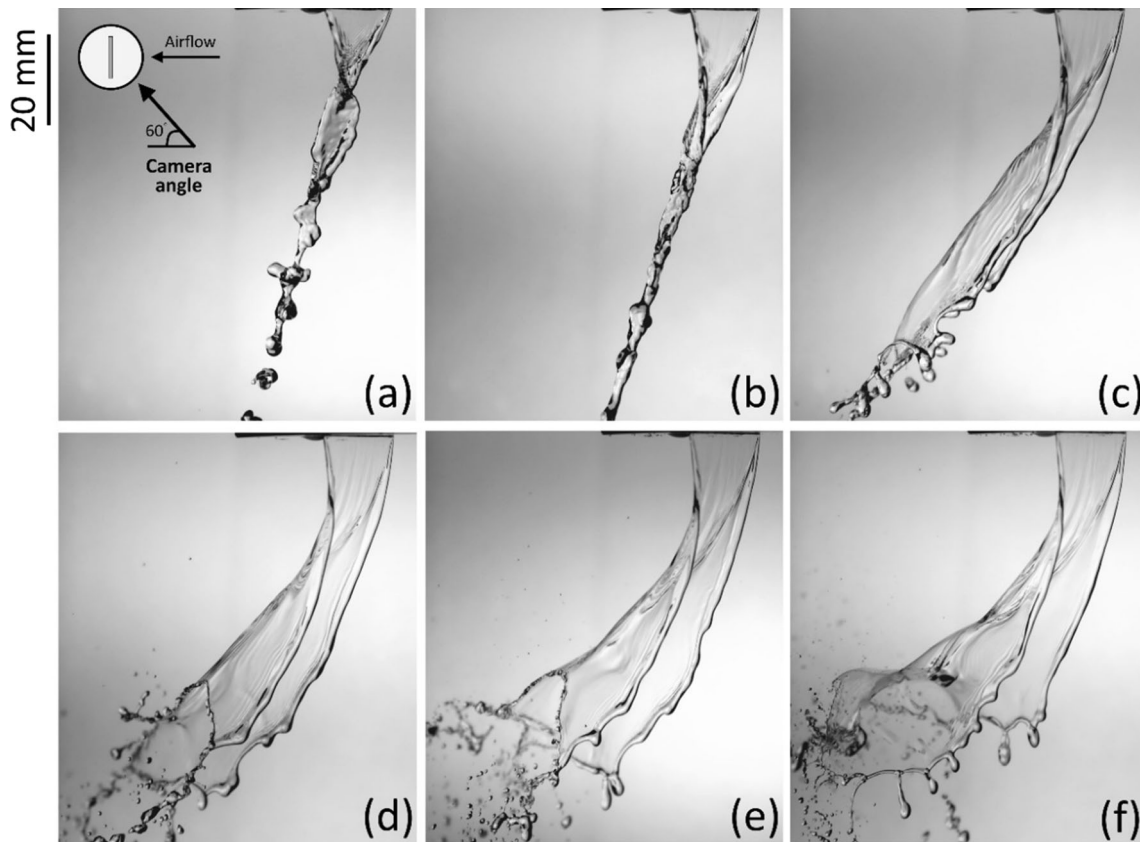


**Fig. 10** Visualizations of inflated sheet development taken from the 60 degree view angle (TD3 sheet at  $q = 100$ ). **a**  $We_j = 4.86$ ,  $We_g = 0.05$ , **b**  $We_j = 9.52$ ,  $We_g = 0.1$ , **c**  $We_j = 15.7$ ,  $We_g = 0.16$ , **d**  $We_j = 23.5$ ,  $We_g = 0.24$ , **e**  $We_j = 28.0$ ,  $We_g = 0.28$  and **f**  $We_j = 32.8$ ,  $We_g = 0.33$

over the rim of the inflated sheet. Further, the growth of RT waves amplitude along the rim was evident. It was noticeable that the bifurcation behavior seen in the TD3 sheet was not identified here. This might be due to the smaller and less expanded inflated sheet that made the distance between the top of the inflated sheet and rims shorter.

With further increase in Weber numbers, the structure of the inflated sheet was perturbed through the appearance of some surface waves. A sequence of these surface waves was captured in Fig. 11d. These waves were first reported by (Ng et al. 2008) for a circular liquid jet injected into gaseous crossflow. Though no explanation was provided about the physics behind these waves, it seemed that they were related to the formation of bags. In Fig. 11e, the consecutive establishment of bags could be seen. As seen, the appearance of bags was simultaneous with the disappearance of the inflated sheet structure. Indeed, the inflated sheet was metamorphosed into a series of bags. This observation was in contrast to what was seen in TD3 sheet, where the bags were formed, expanded, traveled downstream and finally collapsed all over the sheet surface.

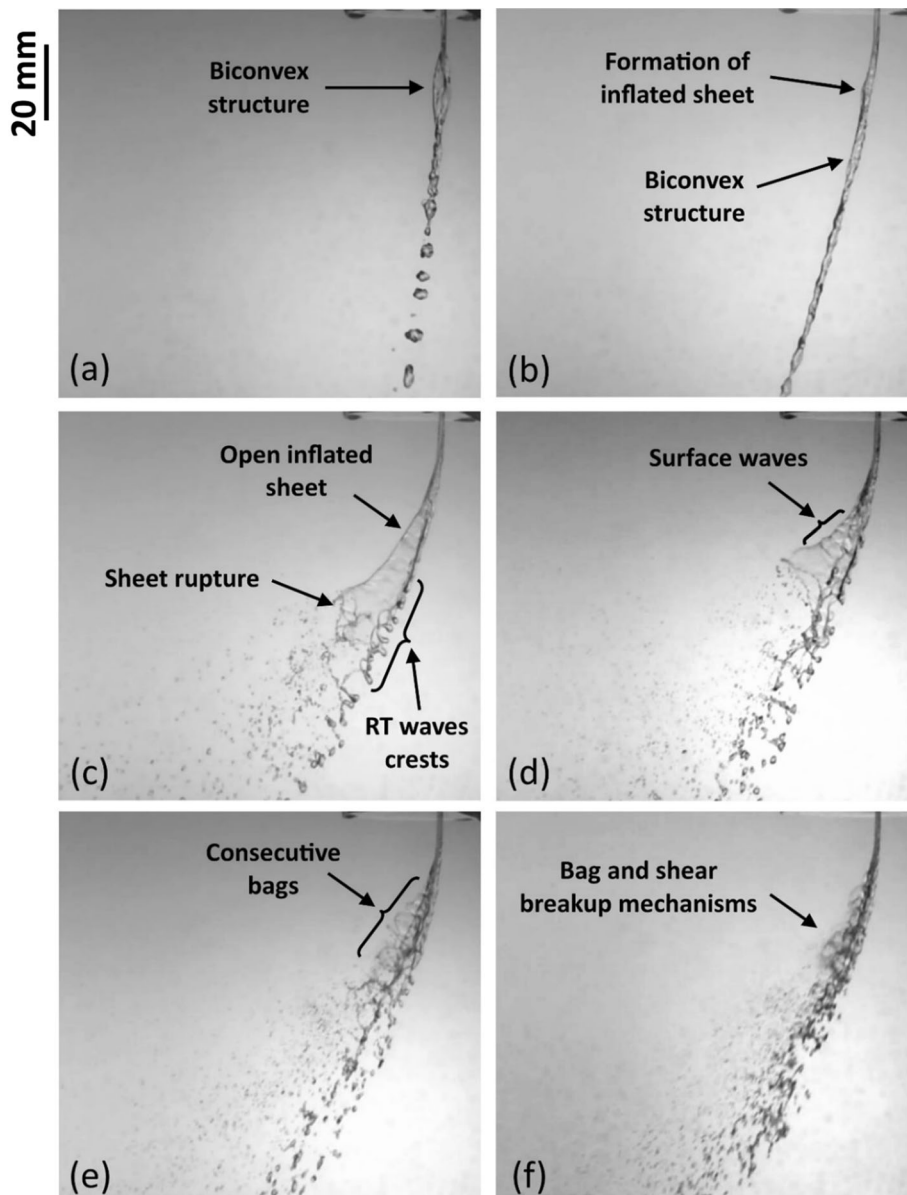


**Fig. 11** Flow dynamics of TD1 sheet at the momentum ratio of 150 and for different Weber numbers. **a**  $We_j = 10.9$ ,  $We_g = 0.07$ , **b**  $We_j = 24.6$ ,  $We_g = 0.16$ , **c**  $We_j = 43.7$ ,  $We_g = 0.29$ , **d**  $We_j = 85.7$  and  $We_g = 0.57$ , **e**  $We_j = 142$  and  $We_g = 0.94$ , **f**  $We_j = 212$  and  $We_g = 1.41$



Finally, in Fig. 11f in which the  $We_g$  was 1.41, the Kelvin–Helmholtz instabilities became significant and surface (shear) breakup was also seen over the liquid flow. At this flow condition, the bag and surface breakup mechanisms both occurred.

The impact of the momentum ratio on the flow dynamics of two-dimensional liquid sheets was also examined. For this sake, the flow of TD1 sheet was visualized at the  $We_j = 212$  and for momentum ratios of 30, 60, 90 and 150. The corresponding visualizations are presented in Fig. 12. The gas Weber number corresponding to each visualization was also provided in the caption since any change of momentum ratio at constant  $We_j$  was feasible by altering the  $We_g$ . According to Fig. 12, it was noticed that the breakup characteristics and the trajectory of the liquid sheets were highly influenced by the momentum ratio. Going from low-to-high-momentum ratios (Fig. 12a–d), the breakup mechanism of the liquid sheet changed from multimode breakup to bag breakup. By decrease in momentum ratio, the aerodynamic effects upon the liquid sheet were strengthened and significantly impacted its breakup features. In Fig. 12a, with the minimum momentum ratio and maximum  $We_g$ , the liquid sheet was transformed into a cloudy region of droplets. At this flow condition, the surface breakup was the dominant breakup mechanism, even though the bag breakup still existed. Surface breakup or shear breakup was resulted by the act of Kelvin–Helmholtz instabilities which were intensified by the increase in air velocity. This instability stripped the liquid particles off from the sheet surface. Further decrease in momentum ratio, would lead to a higher rate of the shear breakup; however, our tests were limited to the minimum momentum ratio of 30. On the other hand, for higher momentum ratios, that were associated with lower air velocities, the formation and collapse of bags became more noticeable. In Fig. 12d that belonged to the momentum ratio of 150, the formation, growth and disintegration of several consecutive bags over the leeward side of the TD1 sheet were easily observable. These bags continued to expand until reaching the maximum size at which the membrane became so thin that the surface tension could not hold it anymore (Ng et al. 2008). Explosion of the bags membrane resulted in the generation of fine droplets that were shed into the upper bound of the fluid flow.

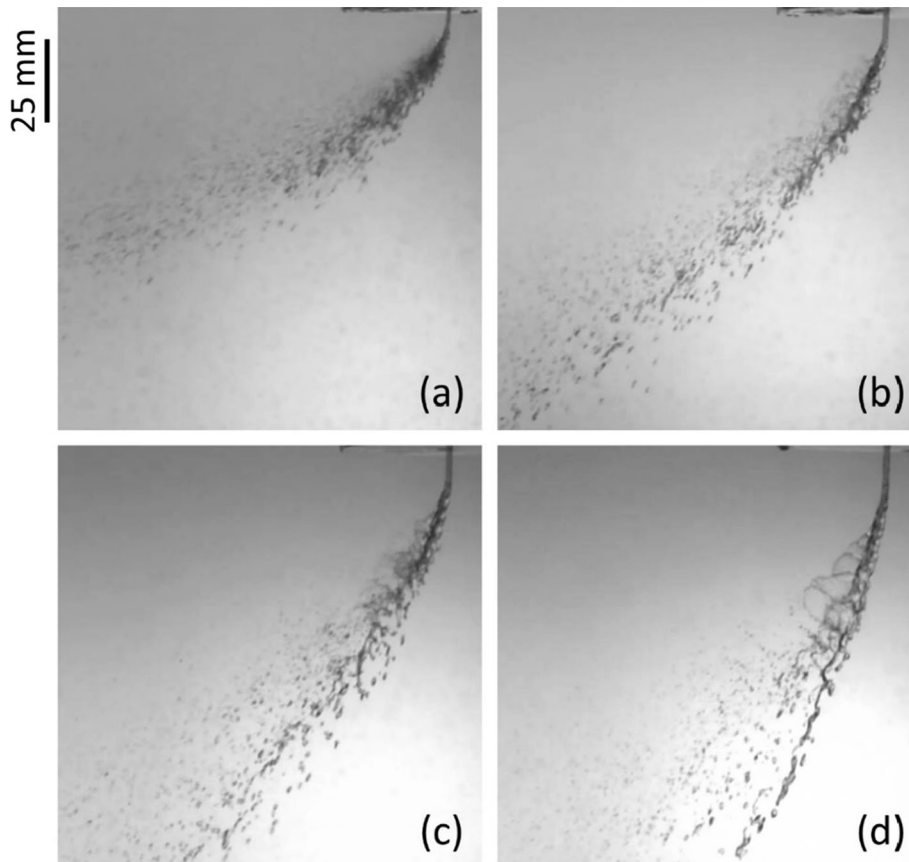


**Fig. 12** Visualizations of TD1 sheet at constant  $We_j = 212$  and for different momentum ratios. **a**  $q = 30$ ,  $We_g = 7.05$ , **b**  $q = 60$ ,  $We_g = 3.53$ , **c**  $q = 90$ ,  $We_g = 2.35$ , and **d**  $q = 150$ ,  $We_g = 1.41$

Moreover, the lower boundary was constructed by ligaments and big droplets that were disintegrated from the sheet due to the work of Rayleigh–Taylor instability.

Trajectory of the liquid sheet was also highly sensitive to the variation of momentum ratio. It can be easily noticed that with the reduction in momentum ratio the liquid sheet was much more bent in the airstream direction. In fact, when the velocity of airflow was increased the aerodynamic force exerted upon the liquid sheet was increased as well; as a result, the liquid sheet was more bent. For Fig. 12a, the drag force on the disintegrated droplets was so strong that they were nearly aligned with the transverse airflow. On the other hand, at high-momentum ratios, the droplets still followed the trajectory of the main liquid flow. This difference came from the fact that at low momentum ratios, the disintegrated droplets were smaller and lighter, therefore readily were influenced by the aerodynamic force. At high-momentum ratios, the droplets were bigger and heavier and could better resist against the airflow.

Flow dynamics of TD1, TD2 and TD3 liquid sheets were also compared to each other in order to examine the effect of aspect ratio. The comparison was provided for two low- and high-momentum ratios; each at two volumetric flow rates. As shown in Fig. 13, the visualizations of all sheets at the momentum ratio of 30 and for volumetric flow rates of 30 L/h and 88 L/h are given. It was revealed that the aspect ratio had a significant effect on the flow features of the liquid sheets. For the  $Q = 30\text{L/h}$ , the inflated sheet was expanded over the TD1 sheet and bags were seen over it. For the TD2 sheet, the inflated sheet was in its early stages of development and was still in the enclosed inflated sheet regime. As shown in Fig. 13c, the inflated sheet was not yet formed for the TD3 sheet and the biconvex structure was clearly present. At the volumetric flow rate of 88 L/h, the TD1 sheet was highly influenced by the airflow and has found a cloudy form due to the high rate of bag and shear breakups. At this  $Q$ , the TD2 sheet was also highly disturbed by different breakup mechanisms, even though shear breakup was absent and bag was dominant. Finally, the TD3 sheet was seen to be in the open inflated sheet, though its surface was disturbed by bags formation and disintegration. Following these visualizations indicated that for liquid sheets with equivalent thickness, decreasing aspect ratio led to the acceleration of liquid flow atomization. Indeed, with the reduction in aspect ratio, the exit surface area and consequently the liquid injection velocity were decreased and increased, respectively (at the constant volumetric flow rate). As a result, at a similar momentum ratio, the gas Weber number and aerodynamic effects were higher for the low aspect ratio sheet.

The comparison was also made for the momentum ratio of 150. In Fig. 14, the visualizations of all sheets for the volumetric flow rate of 30 L/h and 120 L/h are given. The general trend was the same as the

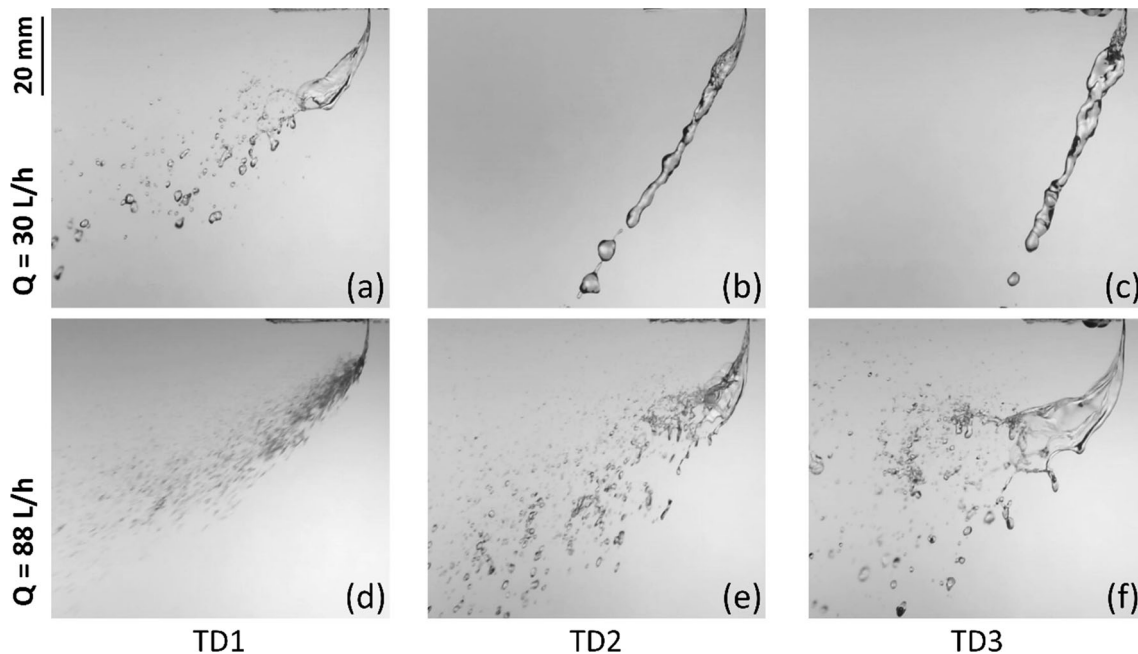


**Fig. 13** Comparison of flow dynamics of two-dimensional liquid sheets at the momentum ratio of 30. For upper row with  $Q = 30\text{L/h}$ : **a**  $We_j = 24.6$ ,  $We_g = 0.82$ , **b**  $We_j = 6.15$ ,  $We_g = 0.2$ , **c**  $We_j = 2.73$ ,  $We_g = 0.09$ . For lower row with  $Q = 88\text{L/h}$ : **d**  $We_j = 212$ ,  $We_g = 7.05$ , **e**  $We_j = 52.9$ ,  $We_g = 1.76$ , **f**  $We_j = 23.52$ ,  $We_g = 0.78$

momentum ratio of 30. For  $Q = 30\text{L/h}$ , the biconvex structure was seen in all sheets, though for TD1 it was much more influenced by the transverse airflow (Fig. 14a). For TD3 sheet the biconvex structure was nearly the same as what was seen in stagnant air (Fig. 14c). For the volumetric flow rate of 120 L/h, the open inflated sheet of TD3 was well-established and no sign of bag breakup could be observed over it (Fig. 14f). However, for the TD2, development of bags was clear and inflated sheet breakup was a combination of both bag breakup and sheet rupture (Fig. 14e). The flow structure of TD1 with the highest gas Weber number was more complicated as the rate of the breakup was intensified and it seemed that the shear breakup was also in action. Following photographs of Fig. 14d–f demonstrated that the size of the inflated sheet was bigger for the TD3 sheet with the highest aspect ratio. It must be noticed that as bigger as the inflated sheets get, the sheet rupture becomes more prominent.

### 3.5 Trajectory of the liquid sheets

The flow development of the two-dimensional liquid sheets in crossflow was comprehensively presented by the aid of visualizations. However, in this final section, the results of sheets trajectory are provided, in order to achieve a quantitative description of the fluid flow. Trajectory is a critically important feature of the liquid flows in crossflow, since it determines the penetration, dispersion and mixing of the liquid with the transverse air in the aeroengine combustors. Analogous to the literature, the lower boundary of the liquid flow was considered as the flow trajectory. In Fig. 15, the measurements of the TD1 sheet trajectory are given for the constant momentum ratio of 90 and at different jet Weber numbers ranging from 10.9 to 296. It must be noticed that in order to keep the momentum ratio fixed, the gas Weber number was increased as well. For the jet Weber number of 10.9, the liquid sheet was bent in airflow direction to some extent, while a bump was clearly observed along the trajectory. This bump was indeed representing the biconvex structure that was seen at low-speed conditions. With escalating the  $We_j$  to 24.6, the biconvex structure was nearly diminished, though the sheet was much more bent. The bending of the liquid sheet can be considered as the competition between the longitudinal inertia of the liquid sheet and the aerodynamic force exerting upon it. Therefore, the increase in bending can be taken as an indication of aerodynamic force intensification. Results of TD1 sheet trajectory at higher Weber numbers revealed that the trajectory formed a final shape and then remained unchanged with further increase in Weber number. Indeed, at high gas and jet Weber

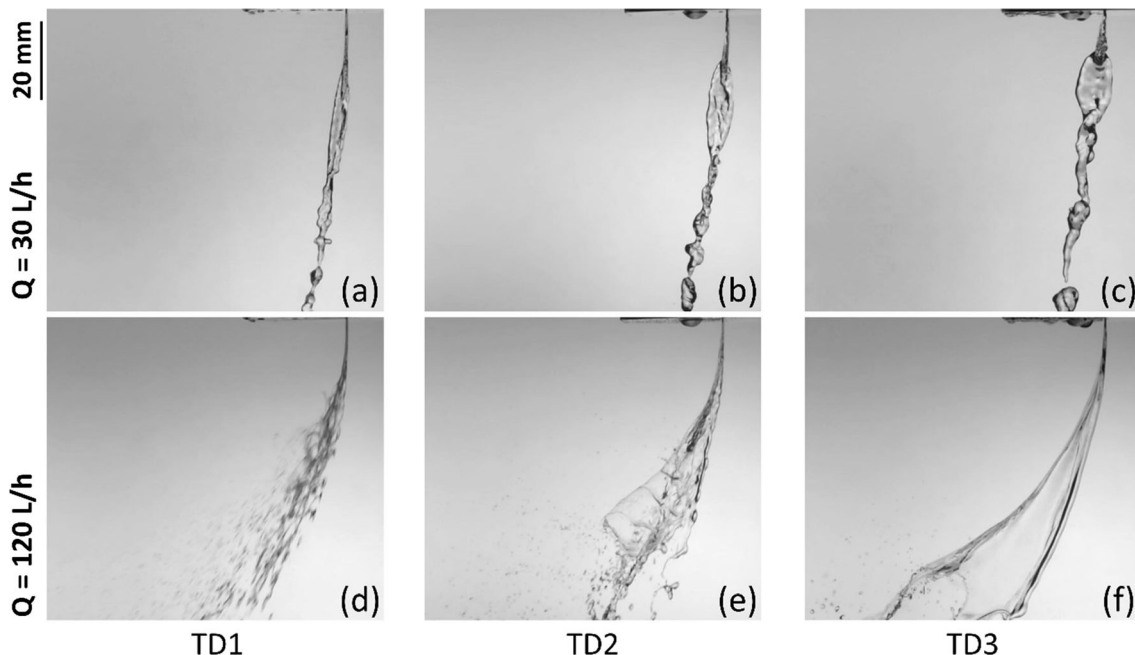


**Fig. 14** Comparison of flow dynamics of two-dimensional liquid sheets at the momentum ratio of 150. For upper row with  $Q = 30\text{L/h}$ : **a**  $We_j = 24.6$ ,  $We_g = 0.16$ , **b**  $We_j = 6.15$ ,  $We_g = 0.4$ , **c**  $We_j = 2.73$ ,  $We_g = 0.02$ . For lower row with  $Q = 120\text{L/h}$ : **d**  $We_j = 394$ ,  $We_g = 2.62$ , **e**  $We_j = 98.4$ ,  $We_g = 0.66$ , **f**  $We_j = 43.7$ ,  $We_g = 0.29$

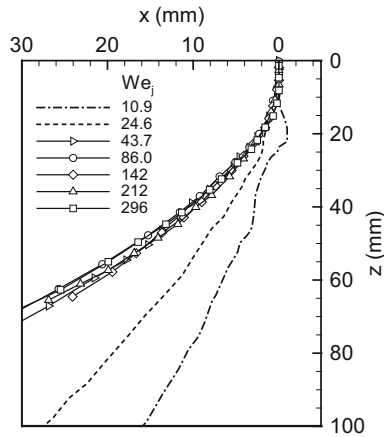


**Fig. 15** Trajectory of TD1 liquid sheet at the constant momentum ratio of 90 and for several Weber numbers

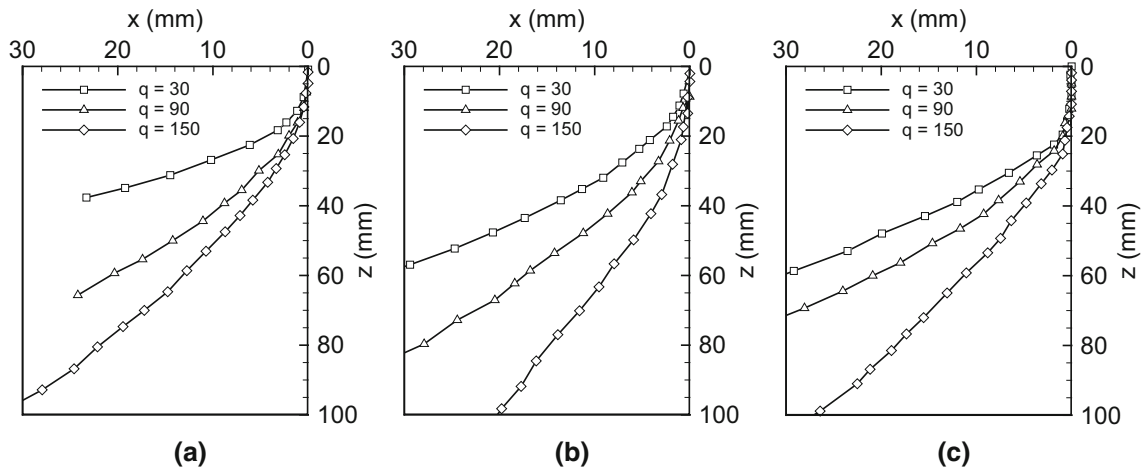


**Fig. 16** Trajectory of two-dimensional liquid sheets at different momentum ratios and constant volumetric flow rate of 72 L/h. **a** TD1 sheet,  $We_j = 142$ , **b** TD2 sheet,  $We_j = 35.4$ , and **c** TD3 sheet,  $We_j = 15.7$

numbers, the sheet inertia and aerodynamic forces achieved an equilibrium. This finding indicated that even though the Weber number was effective in determining the physics of the fluid, its effect on the trajectory was only limited to the low values. It must be noticed that for conventional circular liquid jets, the independency of trajectory from Weber number has been reported in some studies (Bolszo et al. 2014; Wu et al. 1997; Yoon et al. 2011).

To shed light upon the effect of momentum ratio, the measurements of trajectory were conducted for the momentum ratios of 30, 90 and 150, and for the constant volumetric flow rate of 72 L/h, corresponding to the jet Weber numbers of 142, 35.4 and 15.7 for TD1, TD2 and TD3 sheets, respectively. Plots of Fig. 16 revealed a similar behavior between all the three sheets. It was observed that with the decrease in momentum ratio, the liquid sheet was much more bent. Since the  $We_j$  was constant for each sheet, reduction in momentum ratio was obtained by increase in  $We_g$ . As a result, the effects of transverse airflow upon the liquid sheet were intensified and the aerodynamic drag force was increased. It is worth to mention that the same effect of momentum ratio was reported for the conventional circular liquid jets in crossflow (Broumand et al. 2017; Lubarsky et al. 2012).

#### 4 Conclusions

Flow development of two-dimensional liquid sheets in subsonic transverse airflow was experimentally investigated. Three two-dimensional injectors with an equivalent thickness of 0.35 mm and aspect ratios of

30, 60 and 90 were used. The instantaneous physics of the liquid sheets was visualized by the aid of diffused backlight shadowgraphy and high-speed photography. Different view angles were employed for photography in order to achieve a better description of the fluid flow. The flow structure of the liquid sheets was thoroughly investigated for a wide range of momentum ratios ranging from 30 to 500. It was found that the two-dimensional liquid sheets displayed a unique structure that was named as the inflated sheet. This structure completely distinguished the flow characteristics of two-dimensional liquid sheets from circular or other non-circular liquid jets. The aerodynamic force exerted upon the triangular sheet of two-dimensional liquid sheets was responsible for the establishment of the inflated sheet. The inflated sheet was categorized into enclosed and open regimes based on the occurrence of sheet rupture. Moreover, the formation of inflated sheet resulted in a bifurcation in the region of droplets. An upper branch with finer droplets from sheet rupture and bag breakup and a lower branch with bigger droplets from Rayleigh–Taylor instability were observed. A comparison between different liquid sheets with different aspect ratios was also provided at different momentum ratios. It was shown that for lower aspect ratios, the aerodynamic effects became more strong upon the liquid sheet and thus the occurrence of different breakup mechanisms was accelerated. However, the size of the inflated sheet was bigger for TD3 sheet with the highest aspect ratio and therefore sheet rupture had a more prominent role in generating fine droplets. Based on the experimental observations, the flow of two-dimensional liquid sheets in crossflow was phenomenologically categorized into five regimes, biconvex, enclosed inflated sheet, open inflated sheet, bag breakup/sheet rupture and multimode breakup. In the multimode breakup, three breakup mechanisms including bag breakup, sheet rupture and shear breakup simultaneously existed. Furthermore, trajectory of the liquid sheets was measured and its dependency on momentum ratio and Weber number was investigated. Obtained results revealed that Weber number was only effective at low values. Moreover, with increase in momentum ratio, the bending of the sheet was decreased.

## References

- Amighi A, Ashgriz N (2019) Global droplet size in liquid jet in a high-temperature and high-pressure crossflow. *AIAA J* 57:1260–1274
- Amini G, Dolatabadi A (2011) Capillary instability of elliptical liquid jets. *Phys Fluids* 23:084109
- Birouk M, Azzopardi BJ, Stähler T (2003) Primary break-up of a viscous liquid jet in a cross airflow particle & particle systems characterization: measurement and description of particle properties and behavior in powders and other disperse systems. *Particle* 20:283–289
- Bolszo CD, McDonnell VG, Gomez GA, Samuelsen GS (2014) Injection of water-in-oil emulsion jets into a subsonic crossflow: an experimental study. *Atom Sprays* 24:7
- Broumand M, Birouk M (2017) Effect of nozzle-exit conditions on the near-field characteristics of a transverse liquid jet in a subsonic uniform cross airflow. *Phys Fluids* 29:113303
- Broumand M, Birouk M (2019) Liquid jet primary breakup in a turbulent cross-airflow at low Weber number. *J Fluid Mech* 879:775–792
- Broumand M, Rigby G, Birouk M (2017) Effect of nozzle exit turbulence on the column trajectory and breakup location of a transverse liquid jet in a gaseous flow. *Flow. Turbul Combust* 99:153–171
- Chen T, Smith C, Schommer D, Nejad A (1993) Multi-zone behavior of transverse liquid jet in high-speed flow. In: 31st Aerospace sciences meeting, p 453
- Eslamian M, Amighi A, Ashgriz N (2014) Atomization of liquid jet in high-pressure and high-temperature subsonic crossflow. *AIAA J* 52:1374–1385
- Jaberi A, Tadjfar M (2019) Experimental investigation on flow and breakup of two-dimensional liquid jets. In: ASME-JSME-KSME 2019 8th joint fluids engineering conference, 2019a. American Society of Mechanical Engineers Digital Collection
- Jaberi A, Tadjfar M (2019b) Wavelength and frequency of axis-switching phenomenon formed over rectangular and elliptical liquid jets. *Int J Multiphase Flow* 119:144–154
- Jaberi A, Tadjfar M (2020) Comparative study on interfacial oscillations of rectangular and elliptical liquid jets. In: Proceedings of the Institution of Mechanical Engineers, Part G: Journal of Aerospace Engineering, p 0954410019900723
- Jadidi M, Sreekumar V, Dolatabadi A (2019) Breakup of elliptical liquid jets in gaseous crossflows at low Weber numbers. *J Visual* 22:259–271
- Kasyap T, Sivakumar D, Raghunandan B (2009) Flow and breakup characteristics of elliptical liquid jets. *Int J Multiphase Flow* 35:8–19
- Li R, Ashgriz N (2006) Flow and breakup characteristics of elliptical liquid jets. *International Journal of Multiphase Flow* 18:087104
- Lubarsky E, Shcherbik D, Bibik O, Gopala Y, Zinn B (2012) Fuel jet in cross flow—experimental study of spray characteristics. *Adv Fluid Dyn* 59:1
- Muthukumar C, Vaidyanathan A (2014) Experimental study of elliptical jet from sub to supercritical conditions. *Phys Fluids* 26:044104

- Ng C-L, Sankarakrishnan R, Sallam K (2008) Bag breakup of nonturbulent liquid jets in crossflow. *Int J Multiph Flow* 34:241–259
- Pillai DS, Picardo JR, Pushpavanam S (2014) Shifting and breakup instabilities of squeezed elliptic jets. *Int J Multiph Flow* 67:189–199
- Prakash RS, Gadgil H, Raghunandan B (2014) Breakup processes of pressure swirl spray in gaseous cross-flow. *Int J Multiph Flow* 66:79–91
- Sallam K, Aalburg C, Faeth G (2004) Breakup of round nonturbulent liquid jets in gaseous crossflow. *AIAA J* 42:2529–2540
- Song Y, Hwang D, Ahn K (2019) Effect of orifice geometry on column trajectories of liquid jets in crossflows. *Int J Aeron Space Sci* 20:139–149
- Tadjfar M, Jaber A (2019) Effects of aspect ratio on the flow development of rectangular liquid jets issued into stagnant air. *Int J Multiph Flow* 115:144–157
- Tadjfar M, Jaber A, Shokri R (2019) Flow characteristics of rectangular liquid jets injected into low subsonic crossflow. In: *ASME-JSME-KSME 2019 8th joint fluids engineering conference, 2019*. American Society of Mechanical Engineers Digital Collection
- Tan ZP, Bibik O, Shcherbik D, Zinn BT, Patel N (2018) The regimes of twin-fluid jet-in-crossflow at atmospheric and jet-engine operating conditions. *Phys Fluids* 30:025101
- Wang F, Fang T (2015) Liquid jet breakup for non-circular orifices under low pressures. *Int J Multiph Flow* 72:248–262
- Wu P-K, Kirkendall KA, Fuller RP, Nejad AS (1997) Breakup processes of liquid jets in subsonic crossflows. *J Propul Power* 13:64–73
- Wu L, Wang Z-G, Li Q, Li C (2016) Study on transient structure characteristics of round liquid jet in supersonic crossflows. *J Visual* 19:337–341
- Yoon HJ, Hong JG, Lee C-W (2011) Correlations for penetration height of single and double liquid jets in cross flow under high-temperature conditions. *Atom Sprays* 21:1
- Zhang H, Bai B, Wang Y (2018) Quantitative description of droplet dispersion of hollow cone spray in gaseous crossflow. *Exp Thermal Fluid Sci* 93:398–408